Acta Materialia 144 (2018) 68–79

Contents lists available at ScienceDirect

Acta Materialia

journal homepage: www.elsevier.com/locate/actamat

Full length article

Dislocation interactions at reduced strain rates in atomistic simulations of nanocrystalline Al

Maxime Dupraz [a, *], Zhen Sun [a, b], C. Brandl [c], Helena Van Swygenhoven [a, b]

[a] Swiss Light Source (SLS), Paul Scherrer Institut, CH-5232 Villigen PSI, Switzerland
[b] NXMM Laboratory, IMX, École Polytechnique Fédérale de Lausanne (EPFL), CH-1015 Lausanne, Switzerland
[c] Institute for Applied Materials (IAM-WBM), Karlsruhe Institute of Technology, D-76344, Eggenstein-Leopoldshafen, Germany

ARTICLE INFO

Article history:
Received 20 June 2017
Received in revised form
23 September 2017
Accepted 19 October 2017
Available online 25 October 2017

Keywords:
Nanocrystalline materials
Molecular dynamics
Reduced strain rate
Interaction dislocations/grain boundaries

ABSTRACT

Molecular dynamics simulations of transient stress drops have been carried out in different regimes on a nanocrystalline Aluminum sample with average grain size of 12 nm. Besides confirming the interpretation of experimental results obtained during *in situ* X-ray diffraction, the creep simulations performed at 2 or 3 orders of magnitude lower strain rates than usual reveal deformation mechanisms that have not been observed previously. First of all, it is evidenced that the misfit dislocations available at the GB assist the propagation of a lattice dislocation on a plane with low resolved shear stress. Furthermore, it is shown that the interaction of two dislocations gliding on parallel slip planes can result in the emission of a vacancy in the grain interior. Finally, the importance of the Schmid factor in the activation of slip in nanocrystalline structures is discussed.

1. Introduction

It is well established that plastic deformation in nanocrystalline (NC) metals results from the interplay between dislocation and grain boundary (GB) based deformation mechanisms [1–4]. Molecular Dynamics (MD) simulations suggested that GBs act as both source and sink for dislocations [5–13]. A dislocation that is emitted from the GB or triple junction (TJ), travels through the entire grain and can be eventually absorbed in the neighbouring and opposite GBs. As a consequence, dislocation debris are rarely observed in the grain interiors upon unloading (or post-mortem analysis), which is also consistent with the observed suppression of a dislocation network during deformation [14]. Of course, dislocation emission and absorption require also GB accommodation mechanisms and so it is difficult, if not impossible, to separate both type of deformation mechanisms. Atomistic simulations performed for Al and Cu showed a shift from dislocation-mediated plasticity to GB sliding corresponding to a maximum flow strength [8,10,15]. Experimentally, measurements of strain rate sensitivity and flow stress activation volumes confirmed that grain boundary activity is enhanced but not yet dominant in 10 nm grain sized Cu [16] and in 20 nm grain sized Ni-20%Fe alloy [17]. Transmission electron microscopy (TEM) observations in 10 nm grain sized Ni led to the same conclusions [18]. On the other hand, simulations have also suggested that when the grain size is small enough (of the order of 5 nm), plastic deformation could be solely obtained by GB accommodation mechanisms [11,19,20]. Finally, subsequent MD simulations [21] and experimental observations [22] have evidenced that the relative contribution of dislocation glide and GB sliding depend on the amount of plastic strain.

The inherent high strain rates of MD simulations make it however very challenging to determine the rate limiting deformation mechanisms occurring at the much lower strain rates used in experiments. It has been shown that the application of higher strain rates results in higher flow stresses [23,24]: decreasing the strain rate from 5×10^8/s to 5×10^7/s results already in a 15% reduction in the flow stress of NC copper [23]. With these high flow stress, GB accommodation mechanisms are mainly stress driven [24] and dislocations are enabled to propagate athermally through the stress intensities present in GBs. The latter is suggested by the reduced number of cross-slip events at higher strain rates [25,26].

Experimental transient stress-drop tests allow identifying relevant strength contributions of those deformation mechanisms that are not rate-limiting at flow stress levels, but still contribute to the overall strength of the material [22,27,28]. The combination of *in situ* X-ray diffraction and transient stress-drop experiments allow

* Corresponding author.
E-mail address: maxime.dupraz@psi.ch (M. Dupraz).

https://doi.org/10.1016/j.actamat.2017.10.043

to link the kinetic signatures of the deformation mechanisms to their structural footprints. In the diffraction peak analysis, dislocation slip is associated with an increase of the full width at half maximum (FWHM) of the diffraction peak, whereas GB accommodation mechanism are expected to decrease the FWHM [29]. Such experiments have been performed on NC Ni with average grain size of 65 and 35 nm [28]. It was shown that at small stress drops, where the stress dependence of strain rate is high, the FWHM continues to increase due to dislocation-based mechanisms. At large stress drops, recovery mechanisms that reduce the FWHM are dominating and defect recovery mechanisms play an important role in the generation of plastic strain. Interestingly, at intermediate stress drops, the FWHM first decreases and then starts increasing again, suggesting an accommodation of the GBs followed by a re-activation of slip mechanisms.

Inspired by the transient testing experiments we carried out molecular dynamics simulations of stress drops in the regimes similar to those experimentally performed, with the aim to explore the mechanisms responsible for GB accommodation and to verify whether dislocations are still emitted when strain rates after the stress drops are up to 2 or 3 orders of magnitude lower than those usually applied in atomistic deformation simulations. Although still orders of magnitude higher than the experimental strain rates, the contribution of thermally activated processes to the deformation mechanisms [26] and in particular to the GB accommodation mechanisms is indeed expected to be higher at these lower strain rates of 10^6/s.

Our approach confirms the enhancement of the GB accommodation processes at a strain rate of 10^6/s, as well as the slip of dislocations on planes experiencing relatively low resolved shear stress. Additionally, a new GB-dislocation interaction mechanism is evidenced, where the misfit regions available at the GB assist the propagation of a lattice dislocation on a plane with low resolved shear stress. Furthermore, it is shown that the interaction of two dislocations gliding on parallel slip planes can result in the emission of a vacancy in the grain interior. For similar strains obtained with a strain rate of 10^8/s strain rate as usually applied in MD, both mechanisms are not observed and dislocations slip preferentially on high Schmid factor planes.

2. Technical details of the simulation

MD simulation of stress reductions were performed with the open-source Large-scale Atomic/Molecular Massively Parallel Simulator (LAMMPS) [30] on a NC Al sample that contains 15 randomly orientated grains with an average grain size of approximately 12 nm (~ 10^6 atoms) in an orthonormal simulation box of the initial size 27.5 × 27.5 × 27.5 nm^3. The initial sample was geometrically constructed using the Voronoi procedure [31] under full 3D periodic boundary conditions, which are maintained during all simulations. It was then relaxed athermally and equilibrated for 100 ps at 300 K and zero stress MD using the Nose-Hoover thermostat and Parrinello-Rahman barostat [32]. The interatomic interaction was modelled using the Al embedded atom method (EAM) potential of Mishin et al. [33].

The sample was uniaxially loaded with constant strain rate (10^8/s) parallel to the z direction, with lateral zero stress conditions imposed by the Parrinello-Rahman method [34] up to 5.2% total strain. The stress drops were imposed by instantaneous switching to stress boundary condition in the tensile direction.

The structural analysis is performed at instantaneously quenched configurations by viscous damped dynamics for 250 fs at constant simulation box to filter thermal fluctuations. The local crystalline structure is analysed by the common neighbour analysis (CNA) [35], where face centred cubic (FCC) atoms, hexagonal close-packed (HCP) atoms and other coordinated atoms are coloured in grey, red, and blue, respectively. The presence of an intrinsic stacking fault is identified by two consecutive {1 1 1} planes of HCP atoms and a twin fault by only one single {1 1 1} HCP plane. The atomic displacements are corrected by subtracting the simulation box changes to map only the internal, microscopic displacements of atoms. In past work [25,36,37], it has been shown that the local hydrostatic pressure concentrations are sensitive indicator for GB structural changes once dislocation activity occurs, e.g. dislocation emission, pinning, and absorption. In the present work, the local hydrostatic pressure variations within the NC sample are also analysed. This is achieved by calculating the stress tensor of a volume element of radius of 4 Å (as it was done in previous work [25,37]) centred around each atom using the momentum conserving approach derived by Cormier et al. [38]. The open-source software 'Open Visualization Tool' (OVITO) [39] is used to visualize the atomic configurations. The local displacement gradient tensor for each particle within an angstrom cut-off radius corresponding to the distance between the first and second neighbours is used to estimate the local von Mises invariant shear strain. Finally, the dislocation analysis (DXA) [40] as implemented in OVITO and the slip vector analysis method [41] are used in combination to identify and determine the Burgers vector of the dislocations. The line representation of the dislocation defects used in some figures of this manuscript is also computed using the DXA.

3. Results

3.1. Overview of the stress reduction series

Fig. 1 a provides a schematic representation of the stress reduction test. Each specimen is first strained to a pre-defined stress σ_0, and fast unloaded by a certain amount of stress. At the reduced stress σ_r, the specimen is allowed to creep some period of time. The ratio between both stress levels is denoted by the relative reduced stress $R = \sigma_r/\sigma_0$. Fig. 1 b displays the MD simulated stress-strain curve deformed at room temperature at a constant strain rate of 10^8/s. Stress reduction tests series are performed when the sample is strained to an engineering strain of 5.2%, where the flow stress reaches $\sigma_0 = 1.52$ GPa. A wide range of R values was covered from 0.92 to 0.33 similar to the experiments performed in Ref. [28]. After each stress reduction, the specimen was simulated for 1700 ps under constant stress conditions at σ_r. Fig. 1 c displays the corresponding creep strain-time curves. Notably, these curves are found to be stress dependent, and exhibit similar trends as those found in the *in situ* experiments: *i.e.* when the stress drop is mild, there is a continuous forward strain with creep time [28]; when the stress drop becomes larger, an initial anelastic black flow dominates, after which forward strain continues; for the largest stress drop no forward straining is observed within simulated creep time. Fig. 1 d evaluates the number of mobile dislocations propagating during the creep periods for each relative reduced stress R. Dislocation activities including nucleation and propagation are largely suppressed with decreasing R. At moderate stress drops freshly nucleated dislocations can propagate after a certain incubation period. For large stress drops such as $R = 0.53$ and 0.33, nucleated dislocations do not propagate anymore within the time scale of the simulation.

3.2. A medium stress drop with longer creep

The creep strain for the stress reduction with $R = 0.86$ is followed during a longer period of 2290 ps as shown in Fig. 2. In this curve, each pronounced strain burst reflects the propagation of a dislocation across a grain. As expected from a NC material the

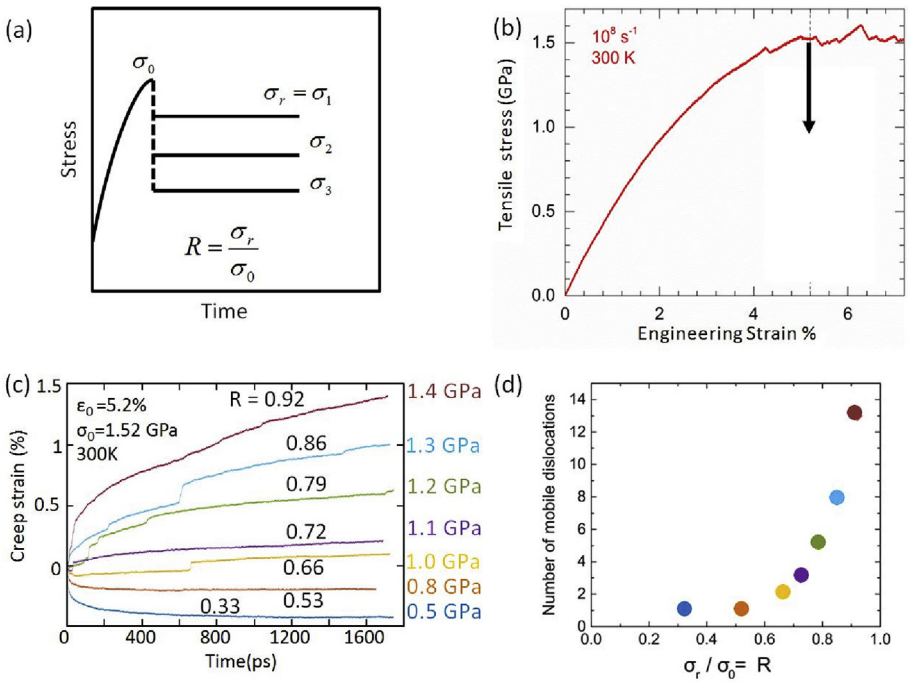

Fig. 1. (a) Schematic representation of a series of conventional stress reduction tests. (b) A simulated stress-strain curve deformed at a constant strain rate of 10^8/s; the stress reduction is performed when the specimen is strained to $\varepsilon_0 = 5.2\%$ and $\sigma_0 = 1.52$ GPa (dotted line). (c) Creep strain-time curves for different R (d) The number of mobile dislocations propagating in the grain interiors for different R.

plastic strain produced by one dislocation per grain is very large, (of the order of b/d ~ 0.1%, b: Burgers vector, d: grain size) [42]. It can be seen that in the initial creep period several slip events occur one after another, respectively in the grains of G13, G2, G10, and G8. As the strain rates gradually decline with creep time, approaching 10^6/s, strain bursts become more separated in time and can be associated with slip events in G9 at $t = 850$ ps and in G14 at $t = 2224$ ps.

3.2.1. Nucleation and slip events in the early stages after the stress drop

In the first 100 ps after the stress drop, slip events are observed in G2, G8, G10 and G13. At this stage of the simulation the strain rates are comprised between 2×10^7/s and 5×10^7/s, *i.e* lower than the initially applied strain rate but still 20 to 50 times higher than the one observed during the slip events in G14 (section 3.2.2). In these grains, all the dislocations are nucleated and propagate using high Schmid factor slip systems: the highest factor for the slip in G2 and G13 and the 2nd highest for G8 and G10. Note that only perfect dislocations are observed to glide in the grains. This is in good agreement with the observations of Zhu et al. [43] and Frøseth et al. [36] who suggested the dominance of full dislocation activity over partial dislocation activity in defect free NC-Al. After a few hundreds of ps, the strain rate has dropped to 3×10^6/s and a strain burst is observed at t = 810 ps corresponding with a slip event using the 2nd highest Schmid factor system (0.42) in G9. The leading partial of the dislocation was nucleated before the stress

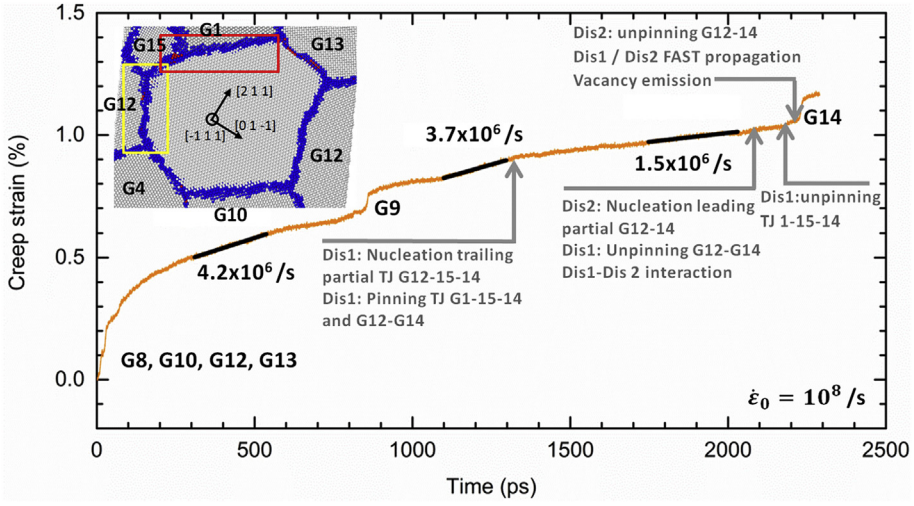

Fig. 2. Creep strain versus time curve for the stress reduction with $R = 0.86$ followed by a creep period of 2290 ps. Each slip event in the sample is indicated. The insert presents G14 (centred) and its neighbouring grains. The viewing direction for G14 is perpendicular to the $(-1\ 1\ 1)$ slip plane. Atoms are coloured based on CNA analysis.

drop and stays pinned at the GB for several hundreds of picoseconds. The trailing partial is observed at t = 530 ps and the full dislocation starts propagating at t = 810 ps. Interestingly, during its propagation a vacancy is emitted and left behind inside the grain. In what follows we focus on the slip event in G14, which occurs at the lowest strain rates after significant GB accommodation using a low Schmid Factor slip system.

3.2.2. Overview of the dislocation activity in G14

The insert in Fig. 2 displays G14 (centred) and its neighbouring grains. The viewing direction for G14 is normal to the (−1 1 1) slip plane. As indicated by the arrows on the creep curve, there are two dislocations Dis1 and Dis2 successively emitted in G14 within a time interval of ~ 800 ps. Until t = 2226 ps the two dislocations travel a limited range (~4 nm) at a reduced speed (~5 m/s) and therefore the strain generated in this time interval is not marked by a strain burst and is mainly issuing from GB accommodation mechanism occurring in the entire sample. The strain burst at t = 2226 ps can be attributed to a remarkable increase of the traveling speed (~900 m/s) of Dis1 and Dis2 enabling them to travel across the grain. A detailed spatiotemporal analysis of dislocation nucleation and propagation was carried out in the rectangular red and yellow regions marked on the insert in Fig. 2. Note that all the GBs between G14 and its neighbours are general GBs with a twist and a tilt component, with the notable exception of G13-G14 which is a vicinal twin boundary.

Fig. 3 displays a series of snapshots showing an overview of the dislocation slip occurring in grain 14, the details will be discussed in following sections. The Thompson tetrahedron in Fig. 3 g is used to indicate the relevant slip planes and Burgers vectors. Immediately after the stress drop (t = 0 ps) GB 12–14 is relatively planar except for two ledges one in region R2 close to the triple junction (TJ) 12-4-14 and another ledge, which is described in more details in section 3.2.2. GB 12–14 contains several dislocation embryos that have been already created during prior loading. However, most of them are reabsorbed in the GB, which is in good agreement with the observations of Asaro and Suresh [44], who suggested that the high stacking fault energy of Aluminium acts as a strong driving force that tends to inverse dislocation motion. Only one dislocation is successfully nucleated as a full dislocation (Dis1) with subsequent propagation into G14 after several nucleation attempts. This dislocation starts to propagate at t = 1318 ps when a trailing partial is emitted from the region R1 nearby TJ 12-15-14. Interestingly, this dislocation has a rather low Schmid factor (0.32) which is only the 5th highest for this grain.

Just after the successful nucleation of the trailing partial dislocation, the full dislocation Dis1 is pinned at TJ 1-15-14 and at a ledge at GB 12–14. Further propagation occurs 750 ps later at t = 2085 ps by dislocation depinning, which is accompanied by the nucleation of the leading partial of another dislocation (Dis2), removing the ledge at GB 12–14. The nucleation of the trailing partial of Dis2 occurs shortly thereafter at t = 2130 ps. The propagation of the full dislocation Dis2 that interacts with Dis1 causes local migration of the GB and the formation of another ledge structure [37]. Inspection of the Burgers vector of the two dislocations reveal that they glide on parallel β planes and possess opposite Burgers vectors: respectively CA and AC for Dis1 and Dis2. They are separated by $2d_{111}$, where d_{111} denotes the interplanar spacing of {1 1 1} planes. Note that the interaction of Dis1-Dis2 forms a jog dragging free volume coming from the GB.

While Dis1 is still pinned at TJ 1-15-14, Dis2 propagates along GB 12–14 until it is pinned again at t = 2175 ps in a region of high compressive stress. Finally, depinning of Dis1 at TJ 1-15-14 and of Dis2 at GB 12–14 occurs at t = 2224 ps. After this last depinning event, the dislocation dipole propagates across the entire grain at a much enhanced speed (900 m/s), resulting in a strain burst visible on the creep curve in Fig. 2. Within 10 ps the dislocations reach the boundaries with grains G10, G12 and G13 where they are eventually absorbed. As a consequence of the fast propagation of the dislocation dipole inside G14, a vacancy is emitted from the jog formed at the intersection between the two dislocations. The details of the aforementioned mechanisms are discussed in the next paragraphs.

3.2.3. Depinning of Dis1 at GB12-14 via nucleation of a lattice dislocation

Inspection of the circled region R1 in Fig. 3 reveals a misfit region across {1 1 1} planes in GB 12–14. At t = 0 ps, this misfit region is delocalized involving 4–5 {1 1 1} planes on both sides of GB 12–14. At t = 1318 ps the misfit region has constricted and Dis1

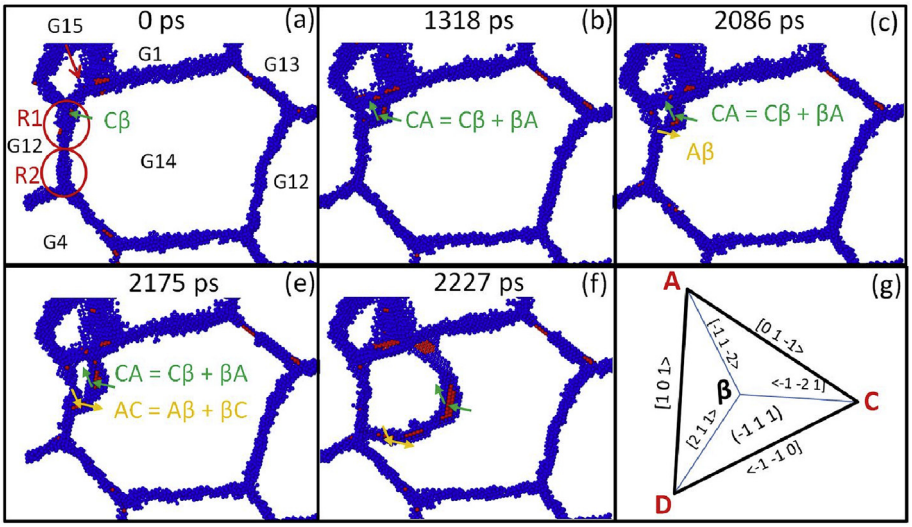

Fig. 3. Evolution of the dislocation activity in G14. The crystallographic orientation of the grain as well as the Burgers vectors of Dis1 and Dis2 are indicated on the figure. Regions showing significant GB activity are circled in red and labelled R1 and R2. Atoms are coloured according to the CNA analysis. To facilitate the visualisation the fcc atoms are omitted. (For interpretation of the references to colour in this figure legend, the reader is referred to the web version of this article.)

starts to propagate [45,46]. However, a ledge in the GB 12–14 acts as a pinning site inhibiting further propagation of Dis1. The configuration of the ledge at t = 2084 is shown and Dis1 is shown in Fig. 4a-c. Pinning of Dis1 is a result of an unfavourable orientation of the Burgers vector relatively to the ledge geometry (Fig. 4c): the ledge representing a step in the direction opposite to the Burgers vector of the leading partial similar to observations in Ref. [37]. Therefore, Dis1 can only further propagate after the removal of the ledge structure shown in Fig. 4 f at $t = 2086$ ps. The latter involves the nucleation of the leading partial of a second lattice dislocation Dis2 with opposite Burgers vector and located 2 lattice planes above the initial dislocation Dis1. As shown on Fig. 4 a-b, where GB 12–14 is seen from the [−2 −1 −1] direction, the nucleation of Dis2 is accompanied by significant atomic shuffling. Inspection of the GB dislocation structure (Fig. 4 c-d) evidences the migration of the grain boundary dislocation (GBD) upon nucleation of Dis2. These local modifications of the GBD structure are associated with the emission of a lattice dislocation as already reported in Refs. [45,46]. The nucleation of Dis2 also induces free-volume migration from the GB in the form of a point defect, which is indicated by a pentagonal shape in Fig. 4 e. This free-volume is dragged at the jog formed by the interaction between Dis1-Dis2 during the initial propagation of the dislocation dipole (section 3.2.4). One can observe in Fig. 4 e-f a relatively high potential energy of atoms (in the β plane) surrounding the point defect (as much as −3.1 eV as compared to the −3.36 eV of the regular fcc atoms). Furthermore, the propagation of the dislocation dipole is accompanied by local migrations of GB 12–14 during in which more ledge structures are formed. Interestingly, part of this migration is recovered as the dislocation dipole glides across the grain as shown in Fig. 5, where the black line indicates the position of the GB before the emission of Dis2. As the dislocations travel across the grain, GB 12–14 first migrates locally by one atomic distance ($t = 2195$ ps where the position of the GB is indicated by a green line). Upon further propagation, this migration is gradually recovered and the GB moves back to its original position ($t = 2196$ ps and $t = 2240$ ps where the position of the GB is indicated by a red line). After depinning from the ledge at G12-G14, the Dis1-Dis2 dipole start to glide slowly (~25 m/s), since Dis1 is still pinned at TJ 1-15-14. After approximately 90 ps of dislocation propagation, Dis2 approaches a region of high compressive local hydrostatic pressures (region R2 in Fig. 3), which act as a pinning site for the dislocation.

Dis2 can eventually overcome this region of high stress intensity by increasing its curvature until it reaches a critical angle with the grain boundary. This is done by the kink-pair nucleation mechanism reported in Ref. [37].

3.2.4. Depinning of the dislocation dipole at TJ 1-15-14

Depinning at TJ 1-15-14 involves a mechanism where the GB misfit structure (or GBD) is used to allow a dislocation to travel along a GB. This mechanism is illustrated in Fig. 6. A view perpendicular to the β plane is provided in Fig. 6 a while Fig. 6 b shows a schematic view of the mechanism for several consecutive time steps. Fig. 6 c shows the slip traces observed on the three β planes. The arrows in Fig. 6 b represent the slip vector of the dislocations on the relevant β planes, while the habit planes of the stacking faults between two partial dislocations are coloured in red. The depinning mechanism is initiated at $t = 2224$ ps by the constriction of full dislocation CA with its Shockley partials Cβ and βA into a perfect screw dislocation (Fig. 6 a). The constriction only occurs in the vicinity of the TJ while the rest of the dislocation remains dissociated, and is immediately followed by a double cross-slip of the constricted dislocation on the adjacent lower β plane, β_{-1}-β_0, as shown by the inversion of the slip traces on the β_0 plane (light green rectangular region in Fig. 6 c). The cross-slip event, at the intersection of the GB with the dislocation, shows the constriction of the two partials into a perfect dislocation prior to cross-slip. It thus falls into the class of Friedel-Escaig [47,48] mechanisms rather than the Fleischer-mechanism [49].

The cross-slip is immediately followed by a partial dislocation nucleation from a misfit dislocation of G1-G14 in the region circled

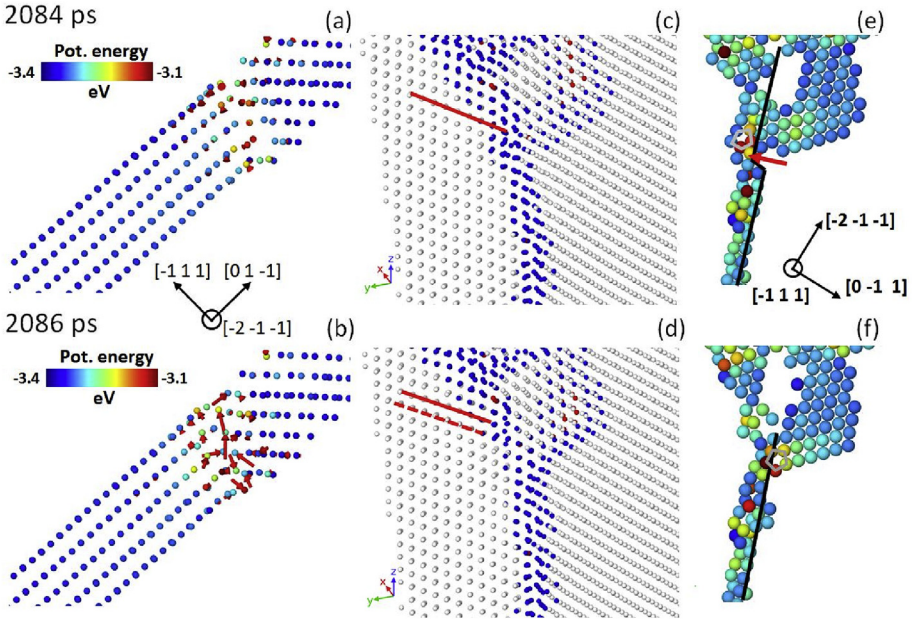

Fig. 4. Removal of the ledge structure assisted by the nucleation of a second lattice dislocation. View of GB 12–14 along the [−1 −2 1] direction before (a) and after (b) the nucleation of the leading partial of Dis2. Location of the GBD before (c) and after (d) the emission of Dis2. The solid line denotes the current position of the GBD and the dashed line its original position. Evolution of the ledge geometry in the habit plane of Dis1 before (e) and after (f) the emission of Dis2. The red arrow indicates the orientation of the Burgers vector of the partial while the solid black line helps the visualisation of the ledge structure. Atoms are coloured according to the CNA in (c) and (d) and to their potential energy in (a),(b)–(e),(f). (For interpretation of the references to colour in this figure legend, the reader is referred to the web version of this article.)

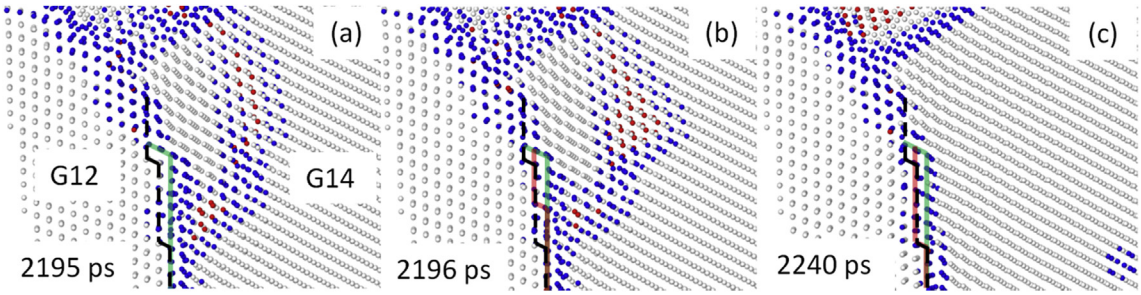

Fig. 5. Local GB migration occurring during propagation of Dis2 creating new ledge structures. Upon further propagation of Dis2 part of the migration of GB 12–14 is recovered. The atoms are coloured according to the CNA analysis. The black dashed line indicates the position of the GB at t = 2080 ps, before the nucleation of Dis2, while the solid green/red line shows the position of the GB at t = 2095ps/2196–2240 ps. (For interpretation of the references to colour in this figure legend, the reader is referred to the web version of this article.)

in purple in Fig. 6 c.

This partial dislocation is nucleated on the γ plane with an Aγ Burgers vector (Fig. 6 b-c). The nucleation of the trailing partial γD, occurs shortly after, resulting in the formation of a dislocation loop AD on the γ plane (Fig. 6 b). Such nucleation of a lattice dislocation from a misfit/GB dislocation has been reported in several MD simulations [45,46] and described analytically [40]. One picosecond later the cross-slipped dislocation and the freshly nucleated dislocation loop react to form a new dislocation CD on the β_{-1}-β_0 plane according to the dislocation reaction CA + AD → CD (Fig. 6 b). In the meantime, the remaining part of the loop cross-slips onto the β_0-β_1 plane (Fig. 6 b-c). This complex dislocation mechanism thus results in the formation of a new dislocation configuration at the vicinity of G1-G14 consisting of two full dislocations AD and CD propagating on two adjacent β planes (shown in Fig. 6 b at t = 2227 ps). Both dislocations immediately dissociate into two sets of partials: βD and Aβ, and Cβ and βD, leading and trailing Shockley partials gliding on the $\beta_0 - \beta_1$ and $\beta_{-1} - \beta_0$ planes respectively. The two leading partials propagating on adjacent β planes create an extrinsic stacking fault (or nanotwin), as indicated from the presence of hcp atoms on planes β_1 and β_{-1} (green rectangular regions in Fig. 6 c). The latter does not extend in the grain but sweeps along the GB and as such helping Dis1 and Dis2 to slip across the grain (Fig. 6 c). The inserts in Fig. 6 c show the slip vectors resulting of the dislocation slip and interactions on the three β planes.

The combination of the slip vectors of the two dislocations gives an overall slip vector in good agreement with the net atomic displacements computed on these planes (Fig. 7 c). In particular it is consistent with the magnitude and the orientation (approximately 3/2βD) of the atomic displacements computed on the β_0 plane.

Table 1 summarizes the dislocation reactions that result in the formation of the dislocation structure consisting of a nanotwin and of two trailing partials Cβ and βD traveling respectively on $\beta_{-1} - \beta_0$ and $\beta_0 - \beta_1$. The spatial arrangement of this dislocation structure shortly after the interaction of the initial dislocation CA with the dislocation loop AD (t = 2227 ps) is shown in Fig. 7 a. Note that after this interaction, the dislocation velocity sharply increases. This fast propagation, despite the presence of ledges at GB 1–14 boundary, can also be explained by simple geometrical considerations. As shown in Fig. 7 a the Burgers vectors of the dislocations forming the dislocation structure at the vicinity of TJ 1-15-14 have a more favourable orientation with respect to the ledge structures at GB 1–14, as compared to the initial dislocation CA. In particular, the trailing partial of the latter, βA, pinned for more than 800 ps at TJ 1-15-14 is transformed by the dislocation reactions described in Table 1. Therefore, the ledge structures which could constitute pinning points for the original dislocation CA are not obstacles for the propagation of the new dislocation structure. Furthermore, the analysis of the local hydrostatic pressure at GB 1–14 (not shown here) reveals the relative absence of regions of stress anomalies that could act as additional pinning sites, the dislocation is thus free to propagate after its depinning from TJ 1-15-14. The local von Mises invariant shear strain on β_0 after the dislocation has swept across the grain (t = 2240 ps) is shown in Fig. 7 b, revealing an important shear trace at the intersection between CA and the nanotwin. Also evident from this picture and from the slip traces on the same plane shown in Fig. 7 b is that the nanotwin and the two partials between the constriction node and GB 1–14 are absorbed back into the GB upon arrival of a larger ledge structure, which happens at t = 2233 ps After the absorption of the dislocation arrangement, the dipole Dis1-Dis2 on the other side of the constriction node recovers its initial configuration and sweeps further across the grain.

The interaction of the dislocation CA with the GB dislocation AD and its subsequent collective propagation induce significant changes the GB ledge structure (cf. Fig. 7 c-d). As illustrated in Fig. 7 e-f, where the atoms coloured in yellow and green indicate the position of the misfit dislocations at t = 2197 ps and t = 2240 ps respectively, this GB-dislocation interaction results in the displacement of the misfit regions by several atomic distances.

3.2.5. *Vacancy emission during dislocation propagation*

The dragging of the jog formed by the Dis1-Dis2 (CA-AC) interaction facilitates the formation of a vacancy inside the grain as shown Fig. 3 e (yellow circle). Further details on this process are shown in Fig. 8 where for different time steps the atomic potential energy of the non fcc atoms in β_1 and β_2 planes (top) and the atomic arrangement in a smaller section of the β planes (bottom) are shown; four different times are selected for the atomic configuration. Here, the colour bar of the potential energy ranges from −3.4 eV (blue) to −3.1 eV (red). As reported in section 3.2.4 a point defect (orange circled) is created at the jog during the initial interaction between Dis1 and Dis2. The analysis of the atomic displacements at GB 12–14, confirms that the formation of this point-defect originates from this GB. As the jog containing the point defect is dragged along with the motion of Dis1-Dis2, e.g. t = 2216 ps, a vacancy is formed and emitted from the jog, see orange circled region at t = 2226 ps. The emission of this point defect cannot be ascribed to a non-conservative motion of the jog, as reported in Refs. [50,51] since the latter glides conservatively on the α plane. The emission of the vacancy results in an energetically more favourable jog configuration, as evidenced by a decrease of the atomic potential energy in the jog at t = 2231 ps.

Fig. 9 a displays the configuration at the time when Dis1 and

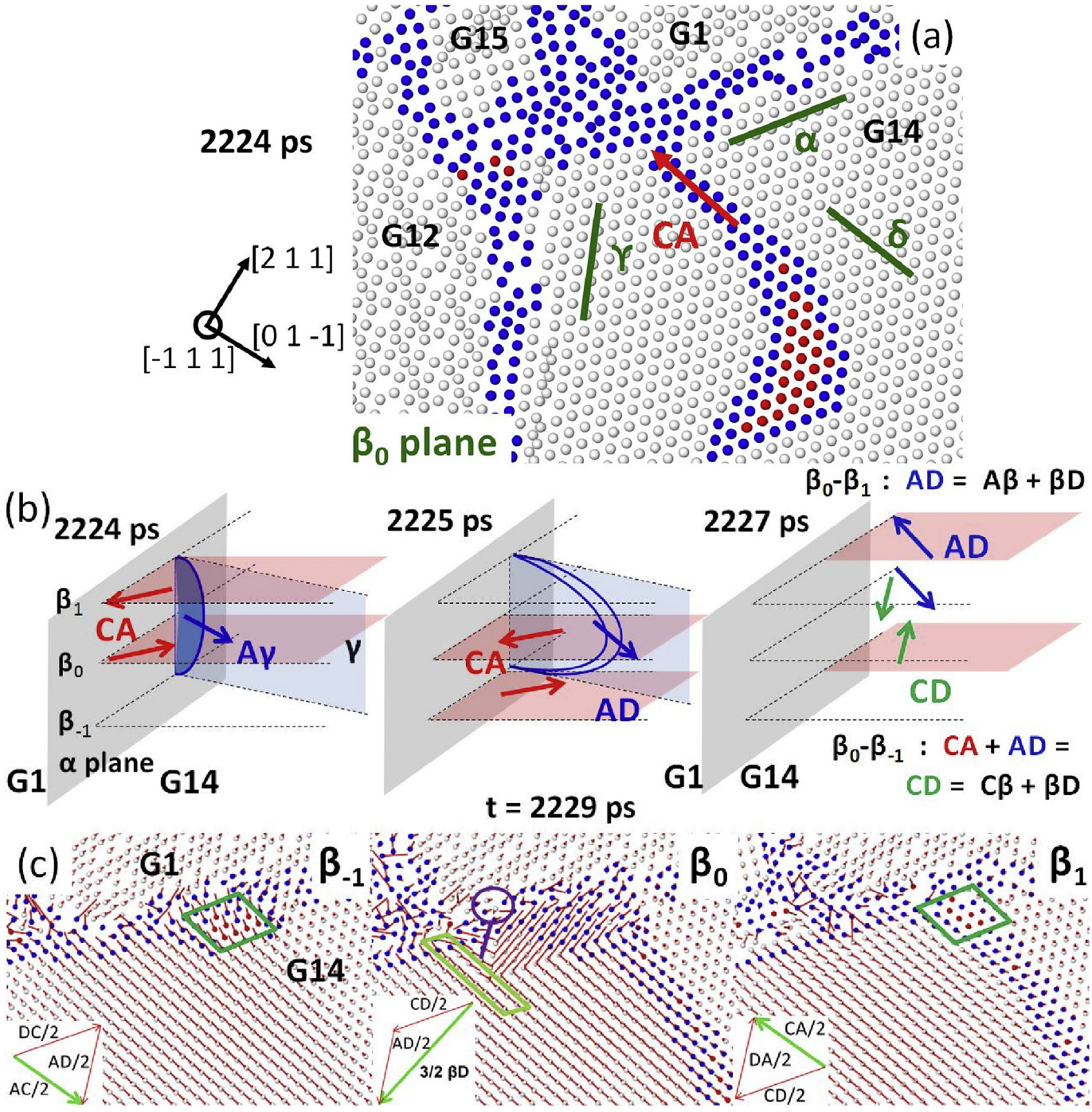

Fig. 6. Closed up view of the perfect screw dislocation CA on the β_0 plane. The Burgers vector of the dislocation is indicated by a red arrow (its actual length is exaggerated to make it better visible), while the green lines denote the relevant {1 1 1} planes. (b) Schematics of the dislocation mechanism at different time steps (see text for details). (c) Atomic displacement vectors on the three β planes at t = 2229 ps. The inserts present the slip vectors of the dislocation on these planes. The atoms in (a) and (c) are coloured according to the CNA. (For interpretation of the references to colour in this figure legend, the reader is referred to the web version of this article.)

Dis2 have been completely absorbed by the neighbouring/opposite GBs (t = 2238 ps). Here only one atomic plane that corresponds to the β_1 slip plane is displayed. The atoms are coloured based on the local von Mises invariant shear strain. It is clearly seen that on the slip plane there are two atomic rows that have relatively high values of von Mises shear strain (in red/yellow colour) as compared to the surroundings. This region in fact corresponds to the slip trace of the jog. The vacancy emission can be correlated to the reduction in shear strain magnitude corresponding to a colour transition from red to yellow for one of the atomic arrays. Further details regarding the change of shear strain in atomic planes above and below is shown in Fig. 9 b. Here a view perpendicular on the slice 1 and 2 along the [0 −1 1] direction (dashed lines in Fig. 9 a) is shown, where slice 1 shows the jog configuration before vacancy emission and slice 2 after emission. A closer look at the slices reveals that the jog undergoes a transition from an obtuse to an acute configuration which has been reported to be more favourable energetically [52].

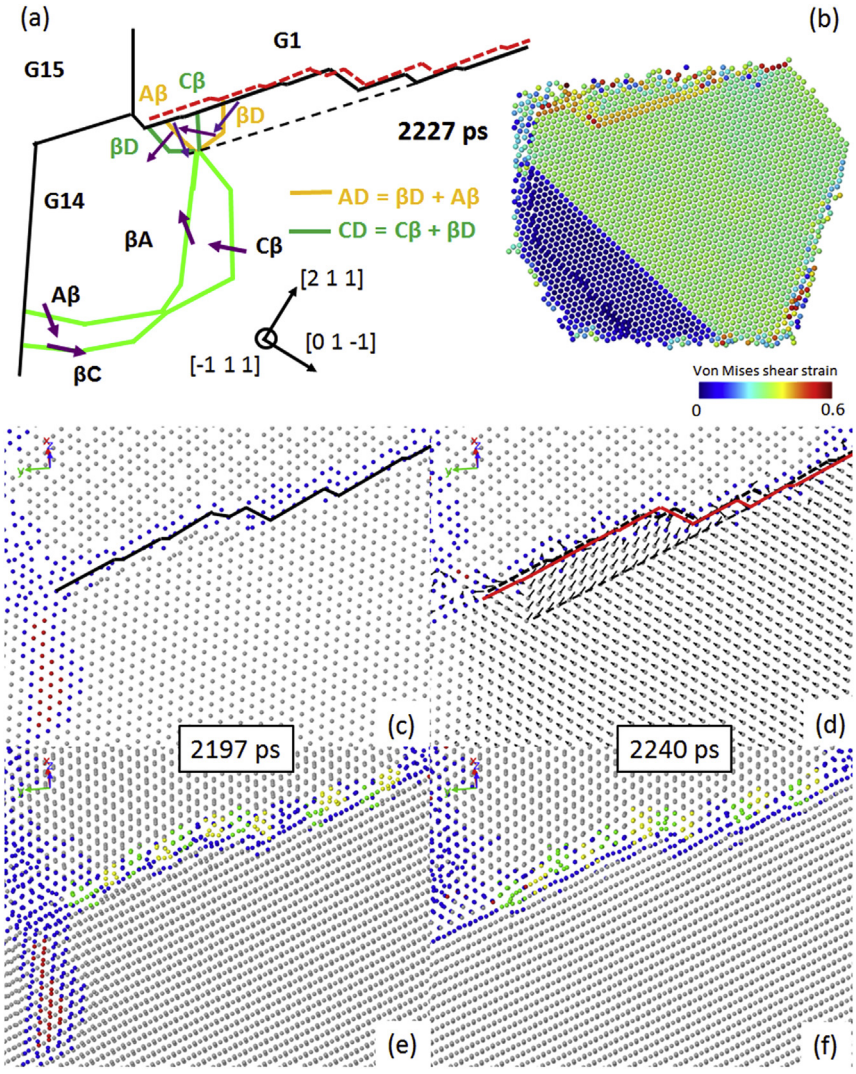

Fig. 7. (a) Schematics of the dislocation configuration after reaction of the impinging dislocation with the dislocation loop nucleated at GB 1–14. (b) Von mises shear strain calculated on the β_0 plane. (a)–(b) Evolution of the ledge structure at GB 1–14 before (t = 2197 ps) and after (t = 2240 ps) the propagation of Dis1 on the β_0 plane. The GB is underlined in black to facilitate the visualization of the position of the ledges. In (b) the dashed black line indicates the initial position of the GB. The computation of the atomic displacement atomic displacement vectors reveals that the dislocation arrangement is absorbed at ledge 4. 8 (c)–(d) Misfit dislocation arrangement at GB 1–14 before and after the propagation Dis1 on the β_0 plane. The atoms coloured in yellow/green indicate the initial/final positions of the misfit dislocations at GB1-14. (For interpretation of the references to colour in this figure legend, the reader is referred to the web version of this article.)

4. Discussion

4.1. Emission of vacancies during propagation

Interestingly, the emission of a vacancy is observed in G9 and G14 where the slip events occur at strain rates < 10^7/s, however using different mechanisms. In G9, the vacancy emission of the vacancy results from the non-conservative motion of a jog. The short jog segment is an edge dislocation, with the line direction and the Burgers vector not contained in its slip plane and therefore can only move by climb. Therefore, a vacancy is emitted during the motion of the jog, a mechanism already observed in MD simulations performed at high strain rates [50,53]. In G14 however, the emission appears to be related to the depinning of Dis1 from the triple junction TJ 1-15-14: after depinning the dislocation moves with a higher speed and releasing free volume in the jog by emitting a vacancy.

Table 1
Overview of the dislocation reactions in G14.

Timestep (ps)	Dislocation	Slip plane
2223	$C\beta + \beta A$	$\beta_0 - \beta_1$
	$\beta C + A\beta$	$\beta_2 - \beta_3$
2224	$CA = C\beta + \beta A$ and $C\beta + \beta A$	$\beta_0 - \beta_1$
	$A\gamma$	γ
	$\beta C + A\beta$	$\beta_2 - \beta_3$
2225	CA and $C\beta + \beta A$	$\beta_{-1} - \beta_0$
	$AD = A\gamma + \gamma D$	γ
	$\beta C + A\beta$	$\beta_2 - \beta_3$
2225	$CD = CA + AD$ then $C\beta + \beta D = CD$	$\beta_{-1} - \beta_0$
	$A\beta + \beta D = AD$	$\beta_0 - \beta_1$
	$\beta C + A\beta$	$\beta_2 - \beta_3$

4.2. Dislocation slip after stress drop: comparison with experiment

In our experimental work [24], stress reduction tests series were performed during *in situ* X-ray diffraction. It was observed that depending on the magnitudes of the stress reduction, the diffraction peak broadening during the subsequent creep periods can either increase or decrease, respectively corresponding to the

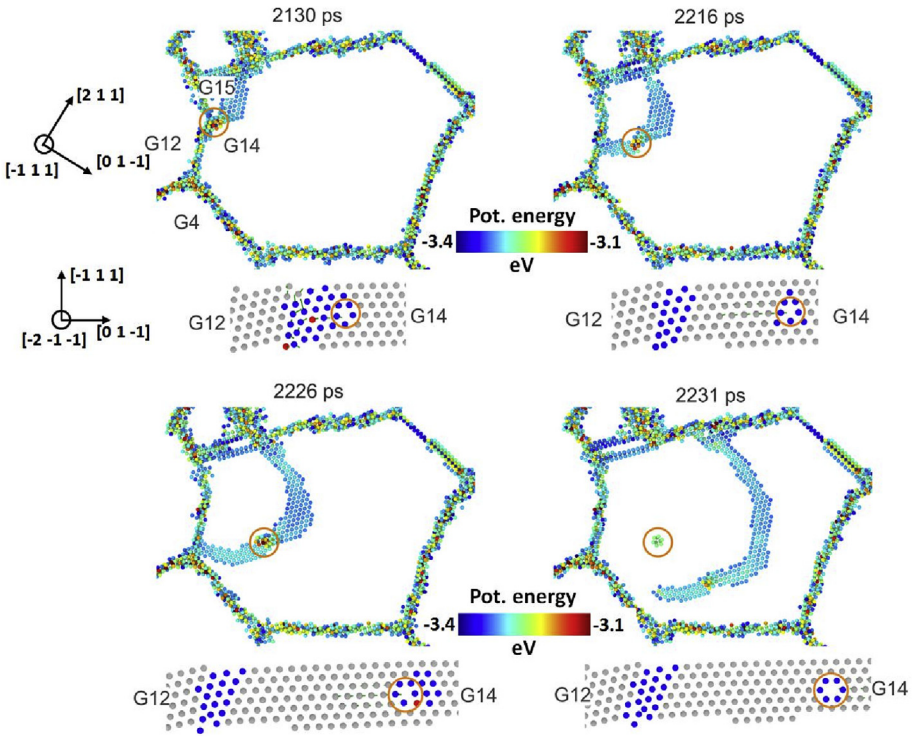

Fig. 8. Emission of a vacancy inside the grain after depinning. The atoms are coloured based on the analysis of atomic potential energy (upper) and CNA (down). The orange circled region shows the formation of a vacancy from a point defect, which is indicative for the free volume migration from the GB12-14. (For interpretation of the references to colour in this figure legend, the reader is referred to the web version of this article.)

dominance of dislocation-based or GB-mediated accommodation mechanism. In the case of a moderate stress drop, the FWHM exhibits a non-monotonic behaviour: after initial reduction the FWHM starts increasing again. This is indicative for re-activated local forward dislocation activity after the dominance of GB accommodation.

The present MD simulations provide a consistent picture: dislocation slip can continue to operate after creep periods up to 1000 ps where the strain rates are considerably reduced by two orders of magnitudes to 10^6/s. It is worth mentioning that the dislocation events in section 3.2 were preceded by modifications of the GB structure: processes such as GB sliding, GB/TJ migration, atomic shuffling, free volume migration, atomic diffusion along the GBs as confinement of delocalized GB dislocations are observed prior to dislocation emission. These GB accommodation mechanisms have been also observed at higher strain rates, however to a lesser extent. The stress drop simulations provide however also an approach to reveal possible mechanisms that have not been seen in atomistic simulations with higher strain rate. These mechanisms are discussed in the next section.

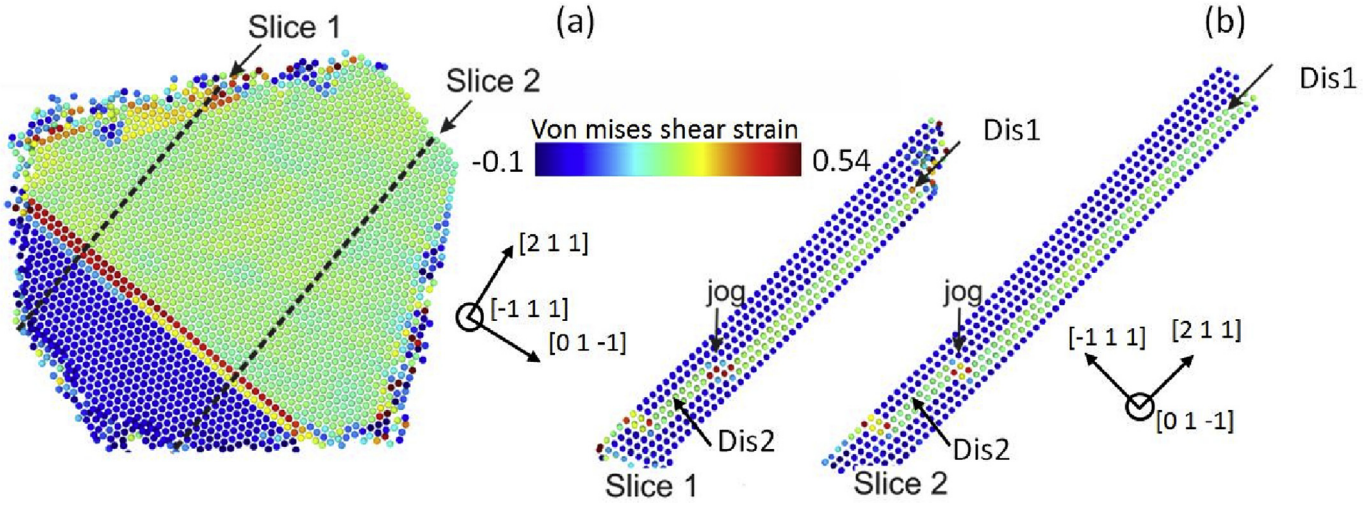

Fig. 9. (a) Shear strain on the β_1 slip plane after Dis1 and Dis2 have been absorbed at the neighbouring/opposite GBs. (b) Two slices at the positions before/after a vacancy emission are selected where the upper/down atomic planes are also inspected.

4.3. The effect of strain rate in MD simulations

4.3.1. Dislocation propagation along a GB

Previous MD simulations focussed on dislocation nucleation and GB accommodation. It is generally accepted that a dislocation once nucleated travels through the entire grain. This has been first observed in MD simulations and analytically described by Asaro et al. [54] and Liao et al. [55]. It has been shown that dislocation can avoid stress intensities in the GB by cross slip [25], a mechanism that is strain rate dependent [26]. It was previously also evidenced that a dislocation can get pinned at a GB ledge structure when for instance the Burgers vector is pointing towards the step in the GB presented by the ledge [37]. At high strain rates further propagation of the leading partial was observed to be facilitated by the nucleation of a kink pairs with the kinks propagating away from each other. The process of kink nucleation continues increases the maximum curvature till a critical angle is reached allowing the dislocation to depin and further propagate, meanwhile depositing a dislocation segment at the GB ledge.

The case studied here is a similar situation, where the direction of the Burgers vector of a propagating dislocation Dis1 is unfavourable for letting the dislocation pass a GB ledge. However, the strain rate is considerably lower (2 orders of magnitude) and the dislocation does not experience the highest possible resolved shear stress. Providing more time, and thus an increased activity in the GBs, allows the GB misfit dislocation and Dis1 to develop a synergetic mechanism: a dislocation loop is nucleated from a misfit dislocation at GB 1–14 and interacts with the impinging dislocation Dis1. This interaction, detailed in sections 3.2.3 and 3.2.4, forms a dislocation structure consisting of two full dislocations, dissociated in two sets of Shockley partials which propagate on two adjacent β planes, below and above Dis1. Note that this dislocation reaction only occurs at the vicinity of GB 1–14, between the GB and a constriction node. The resulting dislocation structure travels along the GB, keeping the initial dislocation Dis1 (CA) away from the GB. This allows the dislocation to travel along the GB, speed up, release of the free volume in the jog, which further accelerates the dislocation. Once the dislocation structure between the constriction node and the GB reaches the next important ledge, the synergetic process ends and the misfit is reinstated at the GB by changing the ledge structure. Dis 1 (still connected to Dis 2) is observed to propagate along the GB without using this synergetic mechanism. The here presented synergetic GB-dislocation process is presumably a thermally activated process, since observation seems to be only possible by the reduced driving forces (e.g. resolved shear stresses) and relative long MD simulation time. This picture is also consistent with previous work pointing towards an increased contribution of thermal assistance in dislocation motion at reduced strain rate [26]. However, one has to remember than 10^6/s is still a very high strain rate, exceeding by orders of magnitude the experimental strain rates. Therefore, despite this increased thermal contribution, the deformation mechanisms are still predominantly stress driven. To assess the role of thermal activation for this deformation mechanism, a systematic study of the stress and temperature-dependence is needed or a direct determination of the associated effective energy barrier. Such a study is certainly needed to conclusively comment on the role and the nature of thermal activation in this complex synergistic deformation mechanism.

4.3.2. Local GB migration

Local GB migration in conjunction with dislocation emission has been frequently observed in MD simulations [8,37,45,46]. Additionally several experimental observations [18,56,57] and MD simulations [58] reported the presence of significant grain boundary motion during plastic deformation involving grain rotation and/or grain coarsening. Such mechanisms are generally observed at large levels of deformation strains in NC metals. Farkas et *al.* [58] concluded that since the temperature in these simulations were performed at 300 K while applying a strain rate of 10^8/s, the process is probably stress derived since there is limited time for thermally activated motion.

The local GB migration shown in Fig. 5 at strain rates that are 100 times slower provides a consistent picture with the observations at high strain rate. However, it is interesting to see that GB motion is partially recovered once Dis2 starts propagating further. This GB migration during the propagation of a lattice dislocation is consistent with the observations of Van Swygenhoven et al. [33]. Such interaction mechanism falls in the category of the GB-dislocation interaction mechanisms, which has been proposed as one of the rate-controlling mechanism in the nanocrystalline regime, and is associated with a low activation volume of 10 b^3 [59].

4.4. Dislocation slip versus GB accommodation

To obtain further understanding of the effect of strain rates on the deformation mechanisms, two atomistic configurations at the same amount of plastic strain of 6.4% are compared: one obtained by continuing the deformation at 10^8/s after 5.2% plastic strain, the other by dropping the stress after 5.2% plastic strain and allowing the material to creep an additional 1.2% strain at rates of the order of 10^6/s.

Table 2 compares their respective number of slip events and deformation time required for the additional 1.2% strain. Without a stress drop, more slip events are observed within a much shorter deformation time suggesting that the relative contribution of dislocation slip to the overall strain is larger than that at the higher strain rates. The analysis of the total strain vs time curve reveals that when the strain rate drops to about 10^6/s, *i.e.* after the strain burst in G9 at t = 900 ps, an additional 0.5% of creep strain is produced during the last 1.4 ns of the simulation.

During this interval of time, the dislocation slip mediated strain is predominantly generated during the strain burst at t = 2224ps in G14, which is of the order of 0.1%. The additional 0.4% creep strain is thus related to GB accommodation mechanisms taking place in the entire sample. In other words, the amount of strain attributed to slip activity at 10^6/s is about 20%. Using a quantitative analysis of plasticity Vo et al. [21] ascribed 55% to dislocation slip in a 15 nm grain size sample deformed with a strain rate of 10^{10}/s till 5% total strain. This tends to confirm the dominance of dislocation slip and lack in GB accommodation mechanisms when using high strain rates in MD simulations.

Table 2: Comparison of the number slip events and deformation time in continuous deformation with and without stress reduction

Table 2
Comparison of the number slip events and deformation time in continuous deformation with and without stress reduction when the same amount of strain is produced.

Deformation mode	Strain produced	Total number of slip events	Deformation time
Without stress drop	1.2%	~10	110 ps
With stress drop		~8	2290 ps

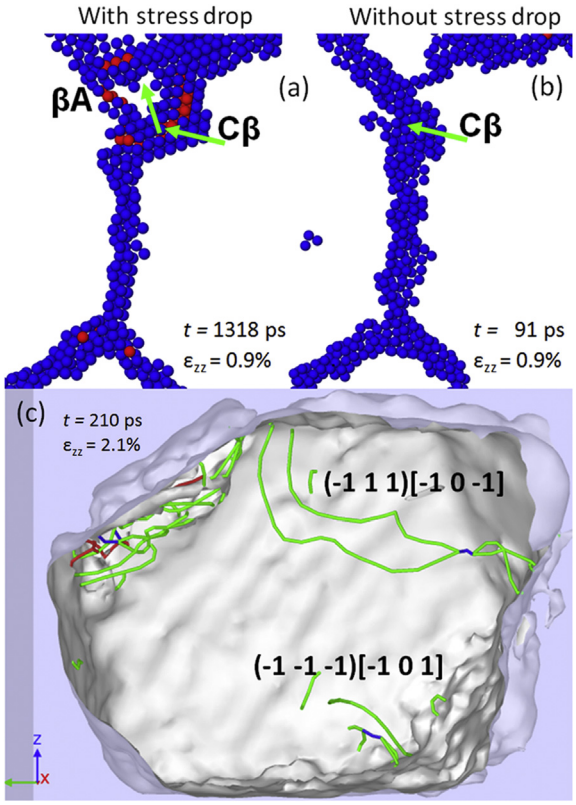

Fig. 10. Comparison at 0.9% additional strain. (a) With the stress drop (b) Without stress drop (c) Dislocation arrangement in G14 after 200 ps at 10^8/s, corresponding to a 2.1% strain.

when the same amount of strain is produced.

We note that the character of the dislocations mentioned in the two simulations is very different. At $t = 1318$, just before the stress drop, one of the partials of Dis1 is already nucleated, but remains very close to the GB. As shown earlier, the trailing partial is nucleated after the stress drop and Dis1 slipped across the grain during the creep strain. Continuing with constant strain rate at the same higher strain rate of 10^8/s instead of a stress drop, however, no trailing partial dislocation is nucleated and there is no other dislocation slip observed in this grain within the 110 ps simulation time needed to reach the additional 1.2% strain (Fig. 10 b). However, continuing straining 210 ps at 10^8/s till 2.1% additional strain, several other slip systems are activated in G14. Fig. 10 c shows these dislocations in G14 analysed with the dislocation analysis (DXA), where the partial/perfect dislocations are coloured in green/blue respectively. The first two slip systems activated: $(-1\,1\,1)[-1\,0\,-1]$ (β/AD) and $(-\,1\,-1\,-1)[-1\,0\,1]$ (δ/BC) have a very high Schmid factor with respective values of 0.488 and 0.459. It thus appears that the high strain rate of the constant strain rate simulation tends to favour the slip system with the highest Schmid factor. Or, in other words, intergranular effects and local GB structural effects seems to play an increased role when lowering the strain rate.

5. Conclusions

Inspired by the experimental transient testing, MD simulations of stress drops were carried out in different stress drop regimes. The creep curves after the stress drops depend on the magnitude of stress drop, and exhibit similar trends as those observed during *in situ* X-ray diffraction experiments *i.e.* dislocation slip can continue to operate after the adaption of the GB structures by a variety of GB accommodation mechanisms. This can explain the non-monotonic behaviour of the FWHM during transient creep where after an initial reduction the FWHM the latter starts increases again. The low strain rates during creep after a stress drop allowed to reveal the furthermore following new mechanisms.

- Lattice dislocations nucleated from misfit dislocations can facilitate cooperative dislocations propagating along a GB with obstacles (i.e. ledges) by interacting temporarily with each other.
- At reduced strain rates (10^6/s), dislocations can propagate using low Schmid factor slip system, a mechanism that requires significant GB accommodation processes.
- A jog resulting from dislocation interactions can drag free volume when the dislocation velocity is relatively low, but will emit a vacancy at higher velocities.

Acknowledgements

HVS and MD gratefully thank the European Research Council for the financial support within the advanced grant advanced grant MULTIAX (339245). ZS gratefully acknowledge the support of the Swiss National Science Foundation for financial support (200021_137881). The MD simulation was performed on the computational resource ForHLR I funded by the Ministry of Science, Research and the Arts Baden-Württemberg and DFG ("Deutsche Forschungsgemeinschaft").

References

[1] T.J. Rupert, Strain localization in a nanocrystalline metal: atomic mechanisms and the effect of testing conditions, J. Appl. Phys. 114 (033527) (2013).
[2] J.R. Trelewicz, C.A. Schuh, The Hall–Petch breakdown in nanocrystalline metals: a crossover to glass-like deformation, Acta Mater. 55 (2007) 5948–5958.
[3] Y. Zhang, G.J. Tucker, J.R. Trelewicz, Stress-assisted grain growth in nanocrystalline metals: grain boundary mediated mechanisms and stabilization through alloying, Acta Mater. 131 (2017) 39–47.
[4] G.J. Tucker, S.M. Foiles, Quantifying the influence of twin boundaries on the deformation of nanocrystalline copper using atomistic simulations, Int. J. Plast. 65 (2015) 191–205.
[5] H.V. Swygenhoven, Grain boundaries and dislocations, Science 296 (2002) 66–67.
[6] H. Van Swygenhoven, J.R. Weertman, Deformation in nanocrystalline metals, Mater. Today 9 (2006) 24–31.
[7] J. Schiøtz, F.D. Di Tolla, K.W. Jacobsen, Softening of nanocrystalline metals at very small grain sizes, Nature 391 (1998) 561–563.
[8] J. Schiøtz, K.W.A. Jacobsen, Maximum in the strength of nanocrystalline copper, Science 301 (2003) 1357–1359.
[9] A.G. Frøseth, P.M. Derlet, H. Van Swygenhoven, Dislocations emitted from nanocrystalline grain boundaries: nucleation and splitting distance, Acta Mater. 52 (2004) 5863–5870.
[10] V. Yamakov, D. Wolf, S.R. Phillpot, A.K. Mukherjee, H. Gleiter, Deformation-mechanism map for nanocrystalline metals by molecular-dynamics simulation, Nat. Mater. 3 (2004) 43–47.
[11] H. Van Swygenhoven, M. Spaczer, A. Caro, Microscopic description of plasticity in computer generated metallic nanophase samples: a comparison between Cu and Ni, Acta Mater. 47 (1999) 3117–3126.
[12] J. Schiøtz, T. Vegge, F.D. Di Tolla, K.W. Jacobsen, Atomic-scale simulations of the mechanical deformation of nanocrystalline metals, Phys. Rev. B 60 (1999) 11971–11983.
[13] P.M. Derlet, A. Hasnaoui, H. Van Swygenhoven, Atomistic simulations as guidance to experiments, Scr. Mater. 49 (2003) 629–635.
[14] A. Kobler, C. Brandl, H. Hahn, C. Kübel, In situ observation of deformation processes in nanocrystalline face-centered cubic metals, Beilstein J. Nanotechnol. 7 (2016) 572–580.
[15] T. Shimokawa, A. Nakatani, H. Kitagawa, Grain-size dependence of the relationship between intergranular and intragranular deformation of nanocrystalline Al by molecular dynamics simulations, Phys. Rev. B 71 (2005) 224110.
[16] J. Chen, L. Lu, K. Lu, Hardness and strain rate sensitivity of nanocrystalline Cu, Scr. Mater. 54 (2006) 1913–1918.
[17] H. Li, H. Choo, P.K. Liaw, The effect of temperature on strain rate sensitivity in a nanocrystalline Ni–Fe alloy, J. Appl. Phys. 101 (063536) (2007).
[18] Z. Shan, et al., Grain boundary-mediated plasticity in nanocrystalline nickel,

Science 305 (2004) 654–657.
[19] H. Van Swygenhoven, D. Farkas, A. Caro, Grain-boundary structures in polycrystalline metals at the nanoscale, Phys. Rev. B 62 (2000) 831–838.
[20] H. Van Swygenhoven, P.M. Derlet, Grain-boundary sliding in nanocrystalline fcc metals, Phys. Rev. B 64 (2001).
[21] N.Q. Vo, R.S. Averback, P. Bellon, S. Odunuga, A. Caro, Quantitative description of plastic deformation in nanocrystalline Cu: dislocation glide versus grain boundary sliding, Phys. Rev. B 77 (2008) 134108.
[22] H. Li, et al., Strain-dependent deformation behavior in nanocrystalline metals, Phys. Rev. Lett. 101 (2008) 015502.
[23] J. Schiøtz, Atomic-scale modeling of plastic deformation of nanocrystalline copper, Scr. Mater. 51 (2004) 837–841.
[24] T. Zhang, K. Zhou, Z.Q. Chen, Strain rate effect on plastic deformation of nanocrystalline copper investigated by molecular dynamics, Mater. Sci. Eng. A 648 (2015) 23–30.
[25] E. Bitzek, C. Brandl, P.M. Derlet, H.V. Swygenhoven, Dislocation cross-slip in nanocrystalline fcc metals, Phys. Rev. Lett. 100 (2008) 235501.
[26] C. Brandl, P.M. Derlet, H.V. Swygenhoven, Strain rates in molecular dynamics simulations of nanocrystalline metals, Philos. Mag. 89 (2009) 3465–3475.
[27] Y.J. Li, J. Mueller, H.W. Höppel, M. Göken, W. Blum, Deformation kinetics of nanocrystalline nickel, Acta Mater. 55 (2007) 5708–5717.
[28] Z. Sun, et al., Dynamic recovery in nanocrystalline Ni, Acta Mater. 91 (2015) 91–100.
[29] S. Van Petegem, S. Brandstetter, B. Schmitt, H. Van Swygenhoven, Creep in nanocrystalline Ni during X-ray diffraction, Scr. Mater. 60 (2009) 297–300.
[30] S. Plimpton, Fast parallel algorithms for short-range molecular dynamics, J. Comput. Phys. 117 (1995) 1–19.
[31] G. Voronoi, Nouvelles applications des paramètres continus à la théorie des formes quadratiques. Deuxième mémoire. Recherches sur les parallélloèdres primitifs, J. Für Reine Angew. Math. 134 (1908) 198–287.
[32] M. Parrinello, A. Rahman, Polymorphic transitions in single crystals: a new molecular dynamics method, J. Appl. Phys. 52 (1981) 7182–7190.
[33] Y. Mishin, D. Farkas, M.J. Mehl, D.A. Papaconstantopoulos, Interatomic potentials for monoatomic metals from experimental data and \textit{ab initio} calculations, Phys. Rev. B 59 (1999) 3393–3407.
[34] Polymorphic transitions in single crystals, A new molecular dynamics method, J. Appl. Phys. 52 (1981) 7182–7190.
[35] J.D. Honeycutt, H.C. Andersen, Molecular Dynamics Study of Melting and Freezing of Small Lennard-Jones Clusters, 2002. Available at: http://pubs.acs.org/doi/abs/10.1021/j100303a014. (Accessed 27 March 2017).
[36] A. Frøseth, H. Van Swygenhoven, P.M. Derlet, The influence of twins on the mechanical properties of nc-Al, Acta Mater. 52 (2004) 2259–2268.
[37] H. Van Swygenhoven, P.M. Derlet, A.G. Frøseth, Nucleation and propagation of dislocations in nanocrystalline fcc metals, Acta Mater. 54 (2006) 1975–1983.
[38] J. Cormier, J.M. Rickman, T.J. Delph, Stress calculation in atomistic simulations of perfect and imperfect solids, J. Appl. Phys. 89 (2001) 99–104.
[39] A. Stukowski, K. Albe, Extracting dislocations and non-dislocation crystal defects from atomistic simulation data, Model. Simul. Mater. Sci. Eng. 18 (085001) (2010).
[40] A. Stukowski, V.V. Bulatov, A. Arsenlis, Automated identification and indexing of dislocations in crystal interfaces, Model. Simul. Mater. Sci. Eng. 20 (085007) (2012).
[41] J.A. Zimmerman, Surface step effects on nanoindentation, Phys. Rev. Lett. 87 (2001).
[42] G. Saada, Hall–petch revisited, Mater. Sci. Eng. A 400 (2005) 146–149.
[43] Y.T. Zhu, et al., Nucleation and growth of deformation twins in nanocrystalline aluminum, Appl. Phys. Lett. 85 (2004) 5049–5051.
[44] R.J. Asaro, S. Suresh, Mechanistic models for the activation volume and rate sensitivity in metals with nanocrystalline grains and nano-scale twins, Acta Mater. 53 (2005) 3369–3382.
[45] H. Van Swygenhoven, P.M. Derlet, A. Hasnaoui, Atomic mechanism for dislocation emission from nanosized grain boundaries, Phys. Rev. B 66 (024101) (2002).
[46] P.M. Derlet, H.V. Swygenhoven, A. Hasnaoui, Atomistic simulation of dislocation emission in nanosized grain boundaries, Philos. Mag. 83 (2003) 3569–3575.
[47] J. Friedel, Dislocations and Mechanical Properties of Crystals, 1957.
[48] B. Escaig, Sur le glissement dévié des dislocations dans la structure cubique à faces centrées, J. Phys. 29 (1968) 225–239.
[49] R.L. Fleischer, Cross slip of extended dislocations, Acta Metall. 7 (1959) 134–135.
[50] S.J. Zhou, D.L. Preston, F. Louchet, Investigation of vacancy formation by a jogged dissociated dislocation with large-scale molecular dynamics and dislocation energetics, Acta Mater. 47 (1999) 2695–2703.
[51] D. Hull, D.J. Bacon, Introduction to Dislocations, Elsevier/Butterworth-Heinemann, 2011.
[52] A.S. Argon, W.C. Moffatt, Climb of extended edge dislocations, Acta Metall. 29 (1981) 293–299.
[53] S.J. Zhou, D.L. Preston, P.S. Lomdahl, D.M. Beazley, Large-scale molecular dynamics simulations of dislocation intersection in copper, Science 279 (1998) 1525–1527.
[54] R.J. Asaro, P. Krysl, B. Kad, Deformation mechanism transitions in nanoscale fcc metals, Philos. Mag. Lett. 83 (2003) 733–743.
[55] X.Z. Liao, F. Zhou, E.J. Lavernia, D.W. He, Y.T. Zhu, Deformation twins in nanocrystalline Al, Appl. Phys. Lett. 83 (2003) 5062–5064.
[56] D.S. Gianola, C. Eberl, Micro-and nanoscale tensile testing of materials, JOM 61 (2009) 24–35.
[57] K. Zhang, J.R. Weertman, J.A. Eastman, Rapid stress-driven grain coarsening in nanocrystalline Cu at ambient and cryogenic temperatures, Appl. Phys. Lett. 87 (061921) (2005).
[58] D. Farkas, A. Frøseth, H. Van Swygenhoven, Grain boundary migration during room temperature deformation of nanocrystalline Ni, Scr. Mater. 55 (2006) 695–698.
[59] M.A. Meyers, A. Mishra, D.J. Benson, Mechanical properties of nanocrystalline materials, Prog. Mater. Sci. 51 (2006) 427–556.